

Detecting Cosmological Phase Transitions with Taiji: Sensitivity Analysis and Parameter Estimation

Fan Huang,^{1,2,*} Zu-Cheng Chen,^{3,4,†} and Qing-Guo Huang^{1,2,5,‡}

¹*CAS Key Laboratory of Theoretical Physics, Institute of Theoretical Physics,
Chinese Academy of Sciences, Beijing 100190, China*

²*School of Physical Sciences, University of Chinese Academy of Sciences,
No. 19A Yuquan Road, Beijing 100049, China*

³*Department of Physics and Synergetic Innovation Center for Quantum Effects and Applications,
Hunan Normal University, Changsha, Hunan 410081, China*

⁴*Institute of Interdisciplinary Studies,
Hunan Normal University, Changsha, Hunan 410081, China*

⁵*School of Fundamental Physics and Mathematical Sciences,
Hangzhou Institute for Advanced Study, UCAS, Hangzhou 310024, China*

Abstract

We investigate the capability of the Taiji space-based gravitational wave observatory to detect stochastic gravitational wave backgrounds produced by first-order phase transitions in the early universe. Using a comprehensive simulation framework that incorporates realistic instrumental noise, galactic double white dwarf confusion noise, and extragalactic compact binary backgrounds, we systematically analyze Taiji's sensitivity across a range of signal parameters. Our Bayesian analysis demonstrates that Taiji can robustly detect and characterize phase transition signals with energy densities exceeding $\Omega_{\text{PT}} \gtrsim 1.4 \times 10^{-11}$ across most of its frequency band, with particularly strong sensitivity around 10^{-3} to 10^{-2} Hz. For signals with amplitudes above $\Omega_{\text{PT}} \gtrsim 1.1 \times 10^{-10}$, Taiji can determine the peak frequency with relative precision better than 10%. These detection capabilities would enable Taiji to probe electroweak-scale phase transitions in various beyond-Standard-Model scenarios, potentially revealing new physics connected to baryogenesis and dark matter production. We quantify detection confidence using both Bayes factors and the Deviance Information Criterion, finding consistent results that validate our statistical methodology.

* huangfan@itp.ac.cn

† zuchengchen@hunnu.edu.cn

‡ huangqg@itp.ac.cn

I. INTRODUCTION

The direct detection of gravitational waves (GWs) by the LIGO and Virgo collaborations [1] has initiated a new era in observational astronomy, providing unprecedented access to astrophysical phenomena that remain invisible to electromagnetic observations. While ground-based detectors operate at frequencies between approximately 10 Hz and 1 kHz, space-based interferometers will explore the milli-Hertz frequency band, where signals from various cosmological sources are expected to be present [2, 3].

One of the potential targets for space-based GW observatories are stochastic GW backgrounds (SGWBs) produced by first-order phase transitions (FOPTs) in the early universe [4, 5]. These transitions occur when a system transitions discontinuously between different vacuum states separated by an energy barrier, resulting in the nucleation and expansion of bubbles of the new phase within the old phase [6–20]. In the Standard Model of particle physics, the electroweak phase transition is crossover-type; however, many well-motivated extensions predict a first-order electroweak phase transition occurring at temperatures of $T_* \sim 100$ GeV [21, 22]. Such phase transitions could explain the observed baryon asymmetry of the universe through electroweak baryogenesis [23, 24], and might be connected to dark matter production mechanisms [25].

The Chinese space-based GW observatory Taiji [26, 27] is one of several proposed missions designed to detect GWs in the milli-Hertz frequency range. Like the European Space Agency’s Laser Interferometer Space Antenna (LISA) [28], Taiji will consist of three spacecraft in a triangular formation, but with arm lengths of 3×10^6 km compared to LISA’s 2.5×10^6 km. The Taiji constellation will follow a heliocentric orbit about 20° ahead of Earth. Another Chinese space-based detector, TianQin [29], is designed with shorter arm lengths of $\sim 10^5$ km and will be in Earth orbit, providing complementary sensitivity in partially overlapping frequency bands.

Detecting the SGWB from FOPTs requires distinguishing this cosmological signal from foreground sources, primarily from galactic and extragalactic compact binary (ECB) systems. The unresolved population of double white dwarf (DWD) binaries in our galaxy forms a significant confusion foreground [30, 31], while the superposition of signals from ECB coalescences contributes an additional stochastic background [32, 33]. The Taiji mission, with its specific noise characteristics and orbital configuration, presents unique capabilities and challenges for separating these components.

The detection of a SGWB from FOPTs faces significant challenges, primarily due to SGWBs contamination from unresolved galactic compact binaries, particularly DWD systems [30, 34], and

from extragalactic compact binaries [35]. Those astrophysical SGWBs are strong enough that they become foregrounds acting as additional “confusion noise” when conducting the detections of other GW signals in same frequency band [36]. Those foregrounds must be carefully modeled and subtracted to reveal primordial signatures [37].

Previous studies have investigated LISA’s capabilities to detect SGWBs from FOPTs [38–45]. More recently, attention has turned to the complementary capabilities of Taiji and the potential for joint observations with LISA or TinQin [46–53]. However, a comprehensive analysis of Taiji’s sensitivity to FOPTs, considering the latest noise models and foreground estimates, remains to be conducted.

In this paper, we comprehensively assess Taiji’s capability to detect SGWBs from FOPTs. Our analysis incorporates detailed modeling of the Taiji noise spectrum, including both instrumental noise and astrophysical foreground contributions from galactic DWD binaries and ECB systems. We implement a Bayesian framework to systematically explore the detectability of phase transition signals across a range of amplitudes and peak frequencies, determining the regions of parameter space where Taiji can make robust detections and provide precise parameter estimates. The paper is organized as follows: In Section II, we present our models for the GW signal from FOPTs, the Taiji detector sensitivity, and the relevant astrophysical foregrounds. Section III describes our Bayesian methodology and simulation framework. Finally, in Section IV, we summarize our findings and discuss their implications for probing beyond-Standard-Model physics with future space-based GW observatories.

II. MODEL COMPONENTS

In this section, we describe the key components of our analysis framework. We first present our model for the GW signal from FOPTs, followed by a detailed characterization of the Taiji detector’s noise properties. We then discuss the two primary astrophysical foregrounds that will impact the detection of cosmological signals: the galactic DWD confusion noise and the ECB background.

A. SGWB from FOPTs

For our analysis of FOPTs as sources of a SGWB, we adopt a simplified broken power-law spectral model obtained from fitting to numerical simulations [11]. The GW energy density is

$$\Omega_{\text{GW}}(f) = \Omega_{\text{PT}} \mathcal{P}(f), \quad (1)$$

where the spectral shape function takes the form of

$$\mathcal{P}(f) = \left(\frac{f}{f_{\text{PT}}}\right)^3 \left[\frac{7}{4 + 3(f/f_{\text{PT}})^2}\right]^{7/2}. \quad (2)$$

Here, Ω_{PT} represents the peak amplitude of the SGWB, and f_{PT} is the peak frequency [11]. The GW power spectrum relates to the power spectral density at the detector through

$$\Omega_{\text{GW}}(f) = \frac{4\pi^2}{3H_0^2} f^3 S_{\text{PT}}(f), \quad (3)$$

where $H_0 = 67.4 \text{ km s}^{-1} \text{ Mpc}^{-1}$ is the Hubble parameter today [54]. The peak frequency depends on the physical parameters of the phase transition:

$$f_{\text{PT}} \simeq 10^{-6} (H_* R_*)^{-1} (T_*/100 \text{ GeV}) \text{ Hz}, \quad (4)$$

where T_* is the temperature at which the phase transition occurs, H_* is the Hubble rate at that time, and R_* is the mean bubble separation.

The f^3 low-frequency behavior is characteristic of phase transitions with mean bubble spacing on the order of the Hubble radius, which produce the strongest signals [19, 20]. The high-frequency f^{-4} behavior approximates the falloff seen in numerical simulations near the peak [11]. This model captures the essential features of FOPT signals while reducing the parameter space to two physically meaningful parameters: Ω_{PT} and f_{PT} . For phase transitions in the temperature range of 100 GeV to 1 TeV (including the electroweak scale and many BSM scenarios), we expect peak frequencies between 10^{-4} Hz and 10^{-2} Hz with peak amplitudes in the range $10^{-14} < \Omega_{\text{PT}} < 10^{-9}$ [40]. These signals fall squarely within Taiji's sensitivity band, making Taiji a promising detector for probing BSM physics through GWs from FOPTs.

B. Taiji noise model

The Taiji space-based GW observatory features three spacecraft in a triangular configuration with 3 million kilometer arm lengths, longer than LISA's 2.5 million kilometers [26, 47]. To extract GW signals from the raw measurements, Taiji employs sophisticated signal processing techniques known as time delay interferometry (TDI) [55, 56]. For our analysis, we focus on the interferometric data streams designated as the X , Y , and Z TDI variables, which represent combinations of phase measurements that substantially reduce laser frequency noise. We adopt several simplifications in our noise modeling approach: 1) we assume that the SGWB signal and instrumental noise are uncorrelated, 2) we model the noise as consisting of two primary components, and 3) we treat all

spacecraft as identical with equal arm lengths forming an equilateral triangle with $L = 3 \times 10^9$ m [57].

The two dominant noise contributions in the Taiji detector can be characterized by their power spectral densities (PSDs). The first component arises from the optical measurement system (OMS), which dominates at higher frequencies (see *e.g.* [58])

$$P_{\text{oms}}(f) = P^2 \times 10^{-24} \frac{1}{\text{Hz}} \left[1 + \left(\frac{2 \text{ mHz}}{f} \right)^4 \right] \left(\frac{2\pi f}{c} \text{ m} \right)^2, \quad (5)$$

where $P = 8$ [59]. The second noise component comes from acceleration noise affecting the test masses, which dominates at lower frequencies

$$P_{\text{acc}}(f) = A^2 \times 10^{-30} \frac{1}{\text{Hz}} \left[1 + \left(\frac{0.4 \text{ mHz}}{f} \right)^2 \right] \left[1 + \left(\frac{f}{8 \text{ mHz}} \right)^4 \right] \left(\frac{1}{2\pi f c} \frac{\text{m}}{\text{s}^2} \right)^2, \quad (6)$$

where $A = 3$ characterizes the acceleration noise level [59].

With these noise components defined, we can express the noise auto-correlation in the X , Y , and Z channels as

$$N_{aa}(f, A, P) = 16 \sin^2 \left(\frac{f}{f_*} \right) \left\{ \left[3 + \cos \left(\frac{2f}{f_*} \right) \right] P_{\text{acc}}(f, A) + P_{\text{oms}}(f, P) \right\}, \quad (7)$$

where c is the speed of light and $f_* = c/(2\pi L)$ defines a characteristic frequency of the detector geometry. The cross-correlation between different channels (*e.g.*, between X and Y) is given by

$$N_{ab}(f, A, P) = -8 \sin^2 \left(\frac{f}{f_*} \right) \cos \left(\frac{f}{f_*} \right) [4P_{\text{acc}}(f, A) + P_{\text{oms}}(f, P)]. \quad (8)$$

For analytical convenience, we transform the X , Y , and Z channels into an alternative basis consisting of the channels A , E , and T

$$\begin{cases} A = \frac{1}{\sqrt{2}}(Z - X), \\ E = \frac{1}{\sqrt{6}}(X - 2Y + Z), \\ T = \frac{1}{\sqrt{3}}(X + Y + Z). \end{cases} \quad (9)$$

This transformation is advantageous because it produces noise-orthogonal channels A and E with identical noise properties, while T functions as a “null channel” with reduced sensitivity to GWs [60]. The noise power spectra in these channels can be derived as

$$N_{A,E} = 8 \sin^2 \left(\frac{f}{f_*} \right) \left\{ 4 \left[1 + \cos \left(\frac{f}{f_*} \right) + \cos^2 \left(\frac{f}{f_*} \right) \right] P_{\text{acc}} + \left[2 + \cos \left(\frac{f}{f_*} \right) \right] P_{\text{oms}} \right\}, \quad (10)$$

and

$$N_T = 16 \sin^2 \left(\frac{f}{f_*} \right) \left\{ 2 \left[1 - \cos \left(\frac{f}{f_*} \right) \right]^2 P_{\text{acc}} + \left[1 - \cos \left(\frac{f}{f_*} \right) \right] P_{\text{oms}} \right\}. \quad (11)$$

To facilitate comparison with astrophysical and cosmological GW signals, we convert the noise spectral densities to equivalent energy spectral densities as

$$\Omega_\alpha(f) = S_\alpha(f) \frac{4\pi^2 f^3}{3H_0^2}, \quad (12)$$

where $\alpha \in \{A, E, T\}$ denotes the channel, and H_0 is the Hubble constant. The noise spectral densities $S_\alpha(f)$ for each channel are defined as

$$S_A(f) = S_E(f) = \frac{N_A(f)}{\mathcal{R}_{A,E}(f)}, \quad (13)$$

$$S_T(f) = \frac{N_T(f)}{\mathcal{R}_T(f)}. \quad (14)$$

Here, \mathcal{R}_α corresponds to the response function for the respective channel α . For this analysis, we employ the analytical expressions for these response functions as derived in [61].

C. DWD foreground

The Milky Way hosts a vast population of DWD binaries, with population synthesis models suggesting approximately $10^7 - 10^8$ such systems throughout our galaxy [62, 63]. These binaries generate gravitational radiation primarily in the frequency band spanning from 10^{-5} to 10^{-1} Hz [64], which overlaps significantly with Taiji’s detection window.

While Taiji will resolve individual signals from the strongest and closest sources, the vast majority of these binaries produce signals below the detection threshold. These unresolved systems generate a collective SGWB that manifests as an additional noise component in the detector, commonly referred to as the “confusion noise” or “galactic foreground” [65]. For a 4-year observation period, this background can be characterized by its spectral density $S_{\text{DWD}}(f)$, which follows a polynomial form in logarithmic space [65]

$$S_{\text{DWD}}(f) = \exp\left(\sum_{i=0}^5 a_i \left(\log\left(\frac{f}{\text{mHz}}\right)\right)^i\right) \text{Hz}^{-1}. \quad (15)$$

This parameterization is valid within the frequency range $10^{-4} < f < 10^{-2}$ Hz, with coefficients $a_0 = -85.5448$, $a_1 = -3.23671$, $a_2 = -1.64187$, $a_3 = -1.14711$, $a_4 = 0.0325887$, and $a_5 = 0.187854$. The corresponding energy density spectrum normalized to the critical density of the universe is given by

$$\Omega_{\text{DWD}}(f) = S_{\text{DWD}}(f) \frac{4\pi^2 f^3}{3H_0^2}. \quad (16)$$

We approximate this galactic background using a broken power-law model

$$\Omega_{\text{DWD}}(f) = \frac{A_1 (f/f_*)^{\alpha_1}}{1 + A_2 (f/f_*)^{\alpha_2}}, \quad (17)$$

The parameters that best fit the detailed population model are $A_1 = 3.98 \times 10^{-16}$, $A_2 = 4.79 \times 10^{-7}$, $\alpha_1 = -5.7$, and $\alpha_2 = -6.2$ [66, 67]. This functional form captures the essential spectral features of the DWD background, particularly the high-frequency steepening that occurs as the number of contributing binaries decreases. This spectral break arises from physical constraints on binary orbital separations, which cannot be smaller than the combined radii of the component white dwarfs.

D. ECB foreground

Beyond our galaxy, the universe contains innumerable compact binary systems that collectively generate a SGWB. This cosmological signal differs fundamentally from the galactic foreground, as it represents the superposition of unresolved binary black hole and neutron star systems distributed throughout cosmic history [68].

While current ground-based interferometers have not yet reached the sensitivity required to detect this background, space-based detectors operating at lower frequencies will probe a different portion of its spectrum. The ECB background is particularly important for understanding the integrated merger history across cosmic time.

For our sensitivity analysis, we model this background with a characteristic power-law frequency dependence

$$\Omega_{\text{ECB}}(f) = A_{\text{ECB}} \left(\frac{f}{f_{\text{ref}}} \right)^{\alpha_{\text{ECB}}}. \quad (18)$$

This spectral shape emerges naturally from the inspiral phase of compact binaries, with the 2/3 power-law index reflecting the frequency evolution of binary systems dominated by gravitational radiation. We adopt an amplitude of $A_{\text{ECB}} = 1.8 \times 10^{-9}$ at the reference frequency $f_{\text{ref}} = 25$ Hz [68].

Unlike the galactic foreground, this background exhibits no spectral breaks within the Taiji frequency band, as the contributing sources span a much broader range of masses, redshifts, and formation channels.

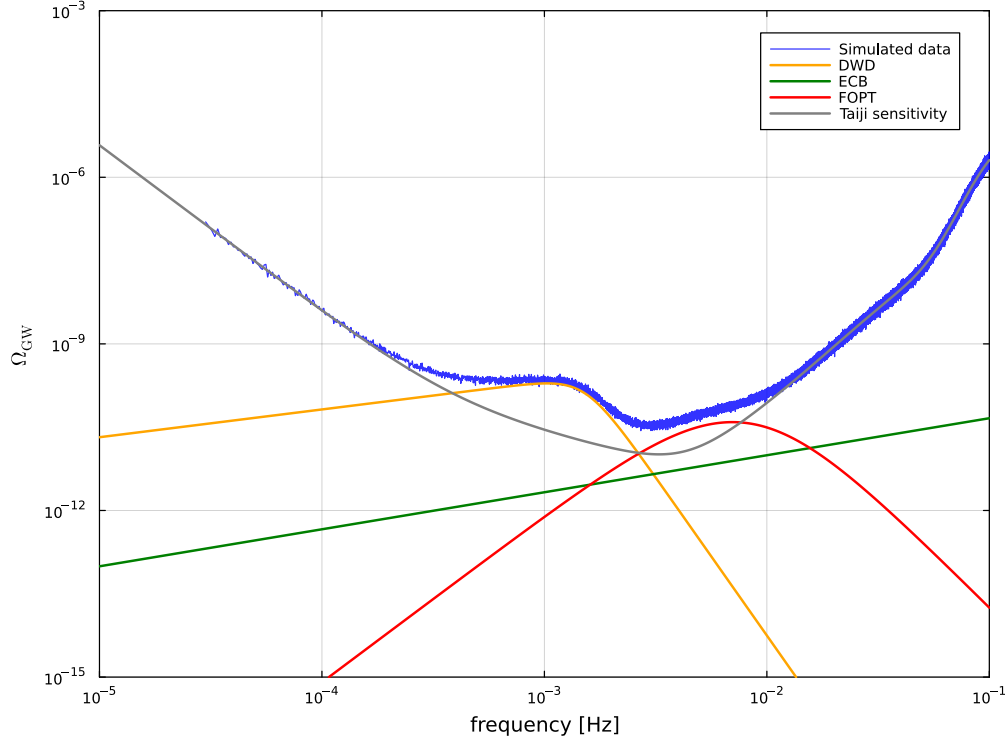


FIG. 1. Frequency-domain representation of synthetic Taiji A-channel observations (blue). We also show the galactic DWD confusion noise (orange), the contribution from ECB (green), and the cosmological background from the FOPT (red) with parameters $\Omega_{\text{PT}} = 3.9 \times 10^{-11}$ and peak frequency $f_{\text{PT}} = 7 \times 10^{-3}$ Hz. For reference, the Taiji detector’s sensitivity is plotted in terms of $\Omega_{\text{GW}}(f)$ as a gray curve.

III. METHODOLOGY AND RESULTS

This section outlines our computational approach for evaluating the Taiji mission’s capability to detect SGWBs from cosmological FOPTs following [69, 70]. Our numerical framework simulates Taiji observations spanning the full 4-year mission duration with realistic duty cycle considerations (75% efficiency), yielding an effective 3-year observations. We segment the TDI measurements into roughly $N_c = 94$ chunks of 11.5 days each [69, 70]. The frequency domain extends from 3×10^{-5} Hz to 0.5 Hz with approximately 5×10^7 total data points at 10^{-6} Hz resolution.

For computational implementation, we transform the time-domain signal into frequency space:

$$d(t) = \sum_{f=f_{\min}}^{f_{\max}} \left[d(f)e^{-2\pi i f t} + d^*(f)e^{2\pi i f t} \right]. \quad (19)$$

Under the assumption of stationarity for both signal and noise components, the Fourier coefficients exhibit the following statistical properties:

$$\langle d(f)d(f') \rangle = 0 \quad \text{and} \quad \langle d(f)d^*(f') \rangle = D(f)\delta_{ff'}, \quad (20)$$

Parameter	Prior	Injected value	Recovered value
A	$\mathcal{U}(2.95, 3.05)$	3	$3.002^{+0.007}_{-0.007}$
P	$\mathcal{U}(7.99, 8.01)$	8	$7.9990^{+0.0013}_{-0.0014}$
$\log_{10} A_1$	$\mathcal{U}(-16, -15)$	-15.4	$-15.39^{+0.04}_{-0.05}$
α_1	$\mathcal{U}(-6, -5.5)$	-5.7	$-5.69^{+0.05}_{-0.05}$
$\log_{10} A_2$	$\mathcal{U}(-6.5, -6)$	-6.32	$-6.31^{+0.04}_{-0.04}$
α_2	$\mathcal{U}(-6.5, -6)$	-6.2	$-6.19^{+0.04}_{-0.04}$
$\log_{10} A_{\text{ECB}}$	$\mathcal{U}(-9, -8.5)$	-8.74	$-8.69^{+0.15}_{-0.18}$
α_{ECB}	$\mathcal{U}(0.5, 1)$	2/3	$0.68^{+0.04}_{-0.05}$
$\log_{10} \Omega_{\text{PT}}$	$\mathcal{U}(-10.609, -10.209)$	-10.409	$-10.408^{+0.004}_{-0.004}$
$\log_{10}(f_{\text{PT}}/\text{Hz})$	$\mathcal{U}(-2.355, -1.955)$	-2.155	$-2.154^{+0.002}_{-0.001}$

TABLE I. Summary of Bayesian analysis results for all model parameters. The table displays the uniform prior ranges (\mathcal{U}) employed in our MCMC sampling, alongside the true parameter values used in synthetic data generation. The rightmost column presents the posterior estimates, showing median values with corresponding 90% credible intervals.

The simulation generates synthetic observations by drawing complex Fourier coefficients from Gaussian distributions characterized by the appropriate power spectral densities. Specifically, at each frequency point, we construct:

$$S_i = \left| \frac{G_{i1}(0, \sqrt{\Omega_{\text{GW}}(f_i)}) + iG_{i2}(0, \sqrt{\Omega_{\text{GW}}(f_i)})}{\sqrt{2}} \right|^2, \quad (21)$$

$$N_i = \left| \frac{G_{i3}(0, \sqrt{\Omega_{\text{A,E,T}}(f_i)}) + iG_{i4}(0, \sqrt{\Omega_{\text{A,E,T}}(f_i)})}{\sqrt{2}} \right|^2. \quad (22)$$

Here, $G_{ij}(M, \sigma)$ represents random samples from a Gaussian distribution with mean M and standard deviation σ . The total power at each frequency combines signal and noise contributions: $D_i = S_i + N_i$. To account for statistical fluctuations, we generate N_c independent realizations $\{D_{i1}, D_{i2}, \dots, D_{iN_c}\}$ at each frequency and compute their ensemble average \bar{D}_i . Fig. 1 illustrates a representative simulated dataset, with injection parameters documented in Table I.

To enhance computational efficiency while preserving information content, we implement adaptive frequency binning. For frequencies below 10^{-3} Hz, we maintain the original resolution, while frequencies between 10^{-3} Hz and 0.5 Hz are rebinned into 1000 logarithmically spaced intervals. This optimization reduces the dataset to 1971 frequency bins per segment. The rebinned data is

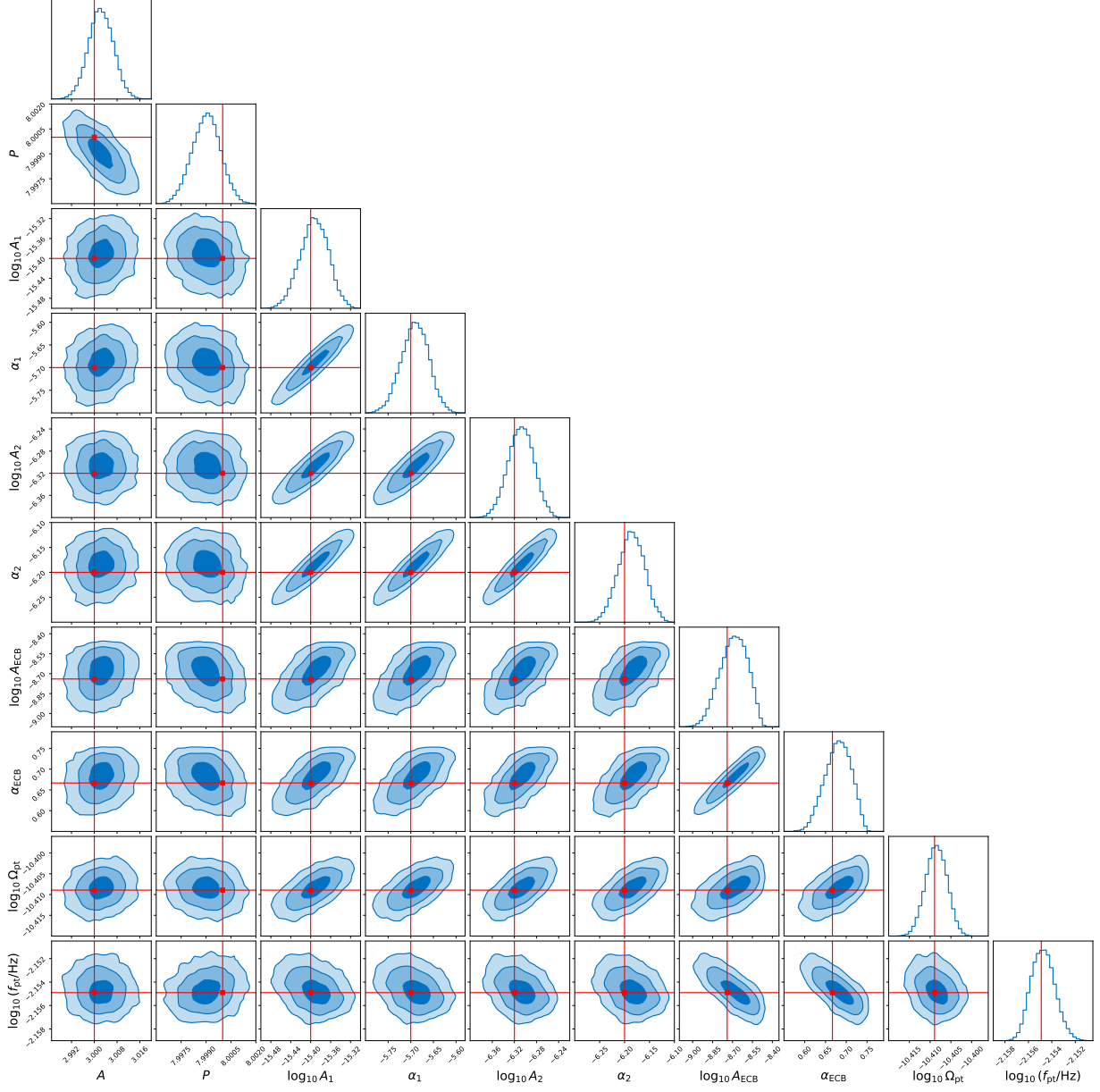


FIG. 2. Posterior distributions of model parameters from Bayesian analysis using simulated Taiji data. The corner plot shows marginalized one-dimensional posteriors along the diagonal and joint two-dimensional distributions with 1σ , 2σ , and 3σ confidence contours in the off-diagonal panels. Red markers indicate the true parameter values used in generating the synthetic signal, which featured a FOPT with amplitude $\Omega_{\text{PT}} = 3.9 \times 10^{-11}$ and characteristic frequency $f_{\text{PT}} = 7 \times 10^{-3}\text{Hz}$.

calculated as:

$$f_k \equiv \sum_{j \in \text{bin } k} w_j f_j, \quad (23)$$

$$\bar{D}_k \equiv \sum_{j \in \text{bin } k} w_j \bar{D}_j, \quad (24)$$

where the optimal weights are

$$w_j = \frac{\mathcal{D}^{\text{th}}(f_j, \vec{\theta}, \vec{n})^{-1}}{\sum_{l \in \text{bin } k} \mathcal{D}^{\text{th}}(f_l, \vec{\theta}, \vec{n})^{-1}}. \quad (25)$$

Our statistical analysis employs a hybrid likelihood function combining Gaussian and log-normal components [70], namely

$$\ln \mathcal{L} = \frac{1}{3} \ln \mathcal{L}_G + \frac{2}{3} \ln \mathcal{L}_{\text{LN}}. \quad (26)$$

The Gaussian part is

$$\ln \mathcal{L}_G(D | \vec{\theta}, \vec{n}) = -\frac{N_c}{2} \sum_{\alpha} \sum_k n_{\alpha}^{(k)} \left[\frac{\mathcal{D}_{\alpha}^{\text{th}}(f_{\alpha}^{(k)}, \vec{\theta}, \vec{n}) - \mathcal{D}_{\alpha}^{(k)}}{\mathcal{D}_{\alpha}^{\text{th}}(f_{\alpha}^{(k)}, \vec{\theta}, \vec{n})} \right]^2, \quad (27)$$

while the log-normal part is

$$\ln \mathcal{L}_{\text{LN}}(D | \vec{\theta}, \vec{n}) = -\frac{N_c}{2} \sum_{\alpha} \sum_k n_{\alpha}^{(k)} \ln^2 \left[\frac{\mathcal{D}_{\alpha}^{\text{th}}(f_{\alpha}^{(k)}, \vec{\theta}, \vec{n})}{\mathcal{D}_{\alpha}^{(k)}} \right]. \quad (28)$$

To quantitatively assess the detectability of phase transition signals, we employ two complementary model selection metrics: the Bayes factor (BF) and the Deviance Information Criterion (DIC). The Bayes factor represents the ratio of evidences between competing models, providing a direct measure of relative model probability. Specifically, we define BF as

$$\text{BF} = \frac{\mathcal{Z}_{\text{FOPT}}}{\mathcal{Z}_{\text{null}}}, \quad (29)$$

where $\mathcal{Z}_{\text{FOPT}}$ is the evidence for the model including a PT component and $\mathcal{Z}_{\text{null}}$ represents the model with only astrophysical foregrounds and instrumental noise. Values of $\ln(\text{BF}) > 8$ indicate decisive evidence favoring the presence of a phase transition signal. As a complementary approach, the DIC incorporates both goodness-of-fit and model complexity through

$$\text{DIC} = D(\bar{\theta}) + 2p_D, \quad (30)$$

where $\bar{\theta}$ represents the posterior mean, $D(\theta) = -2 \ln \mathcal{L}(\theta)$, and $p_D = D(\bar{\theta}) - D(\theta)$ is the penalization term. The difference $\Delta \text{DIC} = \text{DIC}_{\text{null}} - \text{DIC}_{\text{FOPT}}$ provides another measure of model preference, with larger positive values supporting the inclusion of the phase transition component.

Parameter estimation is performed using the nested sampling algorithm implemented in `dynesty`, accessed through the `Bilby` Bayesian inference library. Figure 2 displays the resulting posterior distributions for a representative FOPT signal with amplitude $\Omega_{\text{PT}} = 3.9 \times 10^{-11}$ and characteristic frequency $f_{\text{PT}} = 7 \times 10^{-3} \text{Hz}$. The recovered values, along with their median and 90% equal-tail uncertainties, are also summarized in Table I.

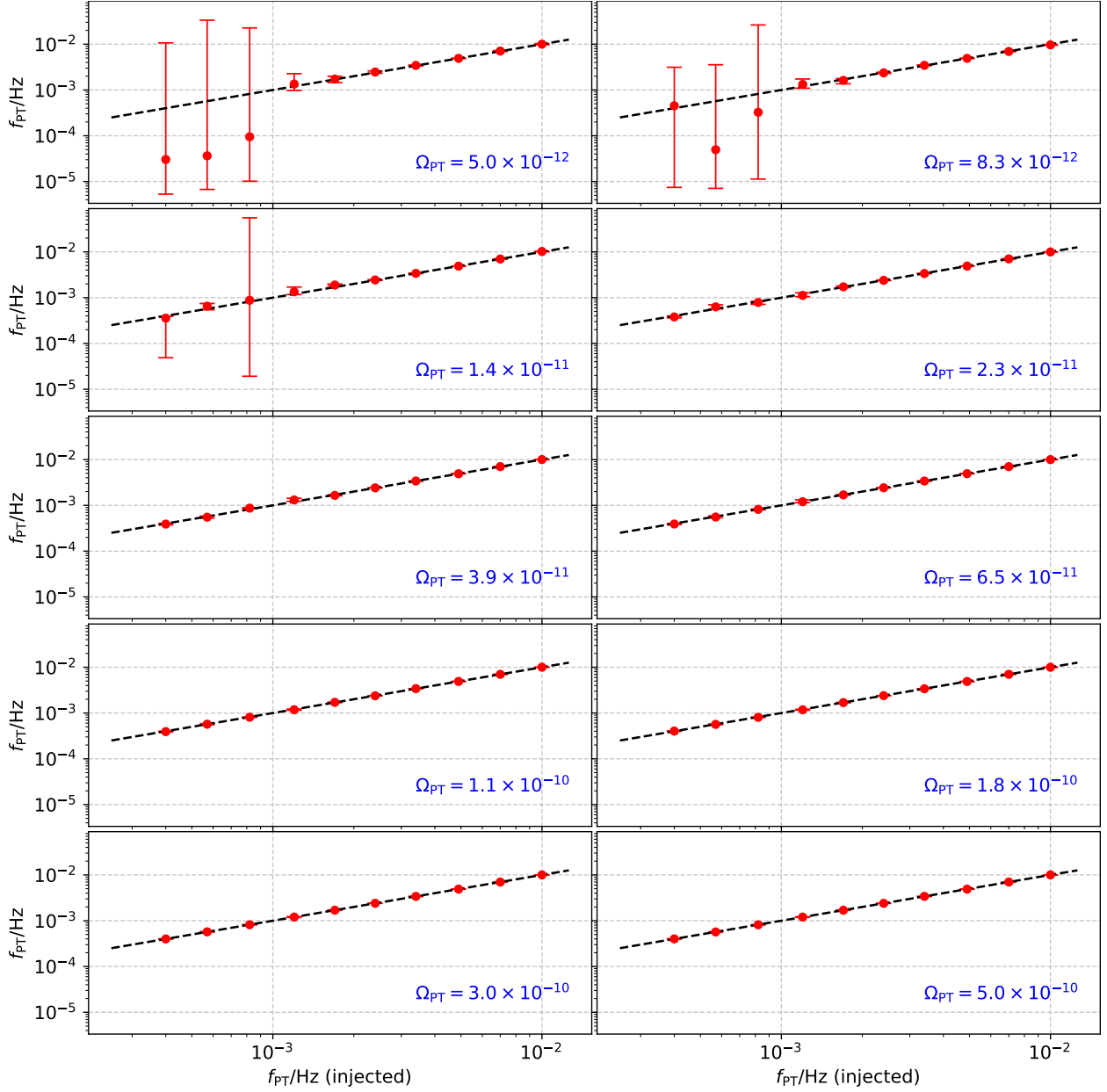


FIG. 3. Comparison between injected and recovered peak frequencies (f_{PT}) of the FOPT signal. Each point represents the median of the posterior distribution, with error bars indicating the 90% credible intervals. The dashed line represents perfect recovery.

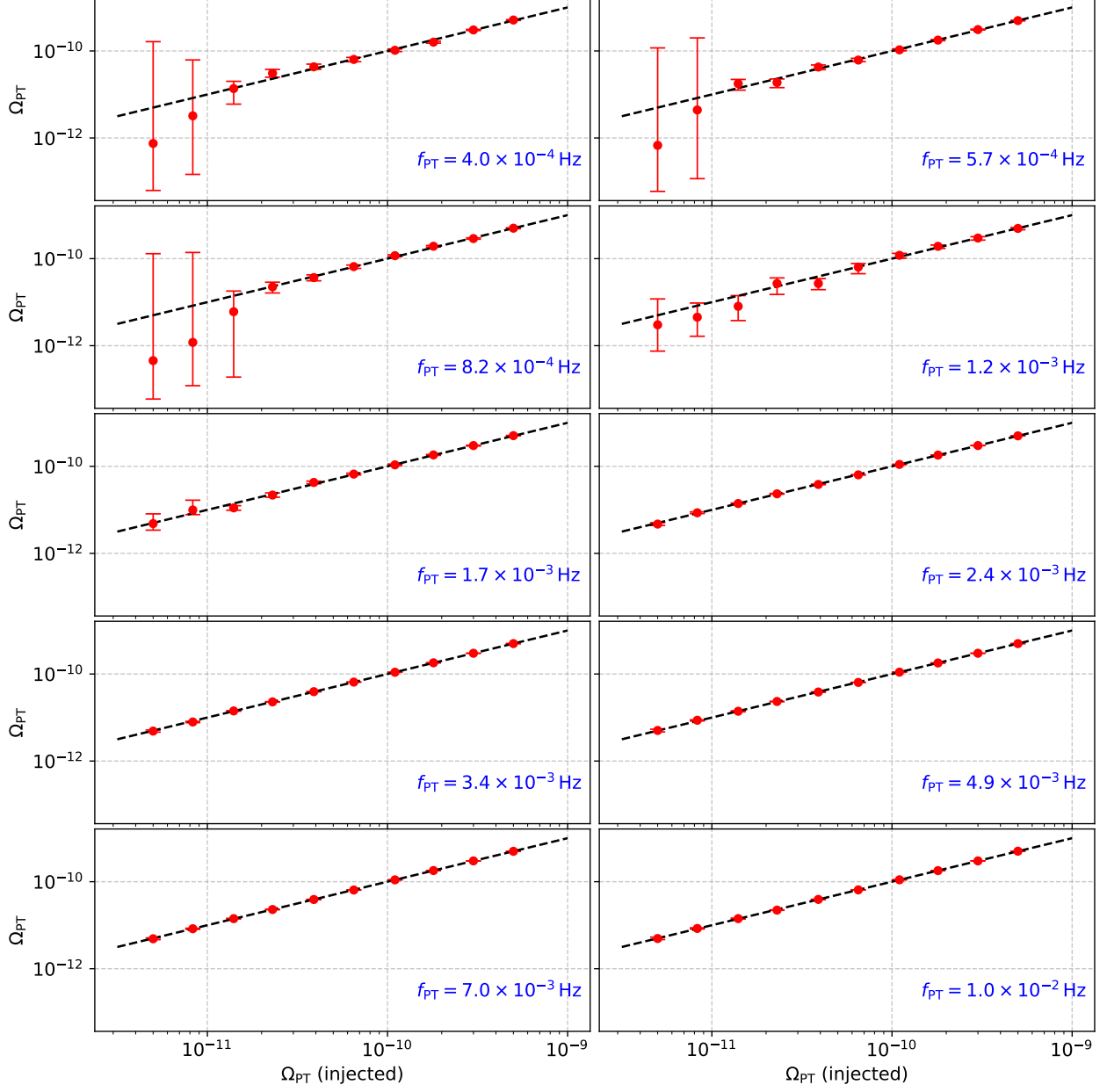


FIG. 4. Comparison between injected and recovered amplitudes (Ω_{PT}) of the FOPT signal. Each point represents the median of the posterior distribution, with error bars indicating the 90% credible intervals. The dashed line represents perfect recovery.

IV. RESULTS AND CONCLUSION

Our simulation framework incorporates a set of base parameters, including: the detector noise characterization parameters fixed at reference values of $A = 3$ and $P = 8$; Galactic foreground modeling with four parameters describing the DWD confusion noise: amplitude coefficients $A_1 = 3.98 \times 10^{-16}$ and $A_2 = 4.79 \times 10^{-7}$, with corresponding spectral slopes $\alpha_1 = -5.7$ and $\alpha_2 = -6.2$;

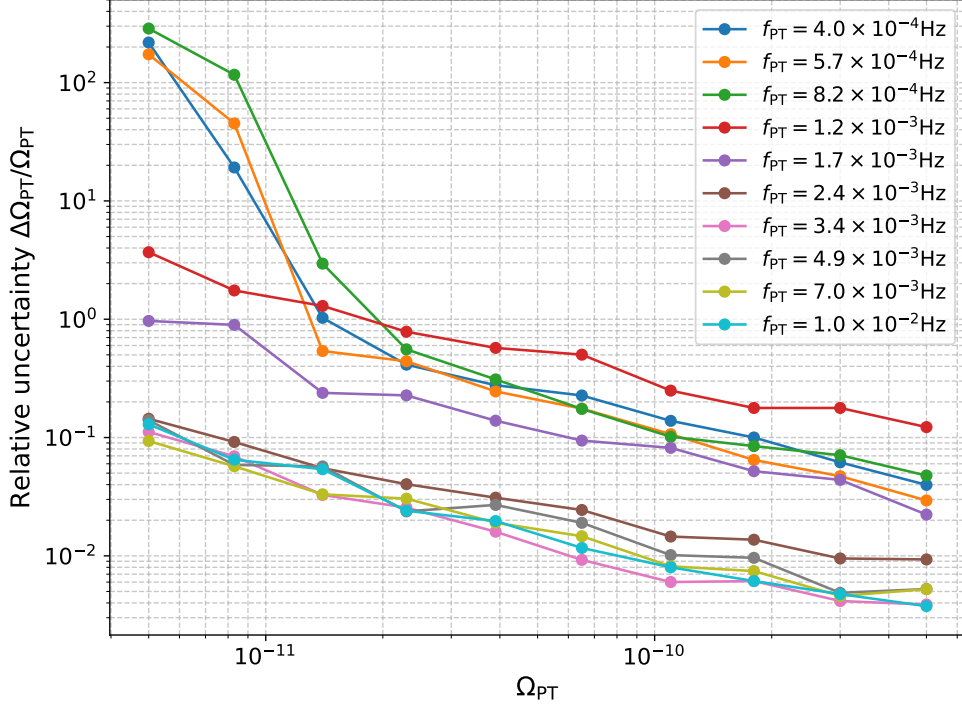


FIG. 5. Measurement precision of the phase transition amplitude as a function of signal strength. The vertical axis shows the relative uncertainty ($\Delta\Omega_{\text{PT}}/\Omega_{\text{PT}}$) in the recovered amplitude, while the horizontal axis displays the injected amplitude values.

ECB background parameterized by amplitude $A_{\text{ECB}} = 1.8 \times 10^{-9}$ with canonical spectral index $\alpha_{\text{ECB}} = 2/3$. While these parameters remain constant throughout our analysis, it is important to note that each simulation represents a distinct statistical realization of the stochastic backgrounds, as the foreground components are characterized by their power spectral densities rather than deterministic waveforms.

Against this realistic background, we systematically inject phase transition signals spanning a two-dimensional parameter grid. The signal strength parameter Ω_{PT} and characteristic frequency f_{PT} are varied across the following ranges:

$$\begin{aligned} \Omega_{\text{PT}} \in \{ & 5.0 \times 10^{-12}, 8.3 \times 10^{-12}, 1.4 \times 10^{-11}, 2.3 \times 10^{-11}, 3.9 \times 10^{-11}, 6.5 \times 10^{-11}, \\ & 1.1 \times 10^{-10}, 1.8 \times 10^{-10}, 3.0 \times 10^{-10}, 5.0 \times 10^{-10} \}, \\ f_{\text{PT}}/\text{Hz} \in \{ & 4.0 \times 10^{-4}, 5.7 \times 10^{-4}, 8.2 \times 10^{-4}, 1.2 \times 10^{-3}, 1.7 \times 10^{-3}, 2.4 \times 10^{-3}, \\ & 3.4 \times 10^{-3}, 4.9 \times 10^{-3}, 7.0 \times 10^{-3}, 1.0 \times 10^{-2} \}. \end{aligned}$$

This parameterization creates a grid of 100 distinct signal configurations, each requiring a separate Markov Chain Monte Carlo (MCMC) analysis. Fig. 1 illustrates the frequency-domain representa-

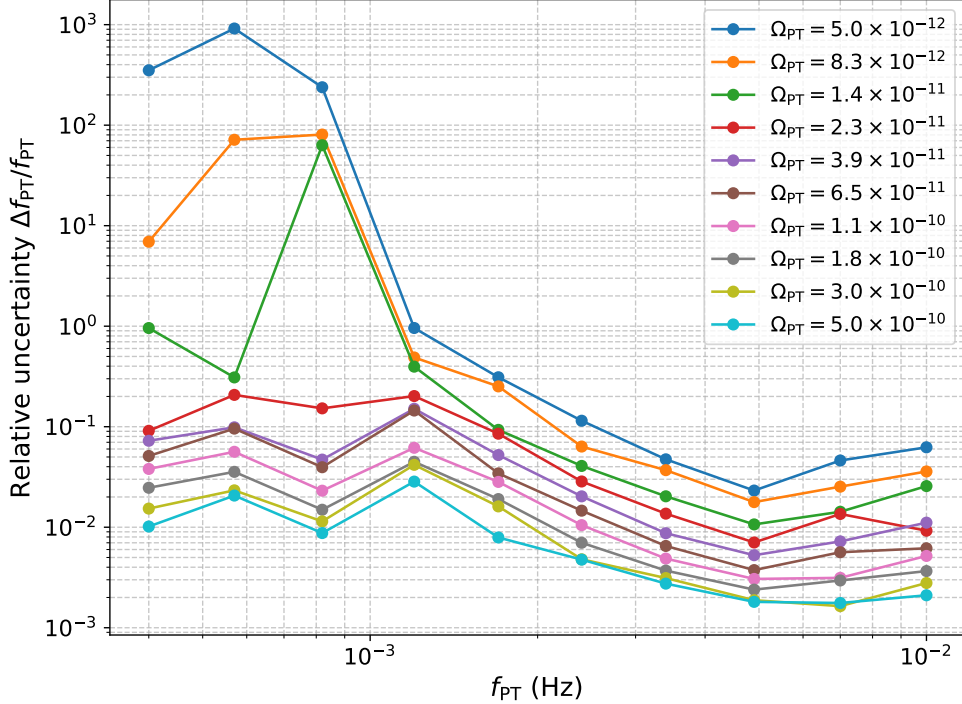


FIG. 6. Frequency resolution capabilities of the analysis pipeline across the detection band. The plot shows the relative uncertainty ($\Delta f_{\text{PT}}/f_{\text{PT}}$) in peak frequency estimation as a function of the injected signal frequency.

tion of synthetic Taiji data for a representative case with $\Omega_{\text{PT}} = 3.9 \times 10^{-11}$ and $f_{\text{PT}} = 7 \times 10^{-3}$ Hz. The corresponding posterior distributions for this benchmark scenario are presented in Fig. 2, demonstrating that all model parameters are successfully recovered within the 2σ credible intervals.

Fig. 3 and Fig. 4 display the measurement uncertainties in the recovered peak frequency f_{PT} and amplitude Ω_{PT} , respectively, across the parameter space. The error bars exhibit significant growth when Ω_{PT} falls below 1.4×10^{-11} or when f_{PT} is less than 1.2×10^{-3} Hz. This degradation in parameter estimation precision can be attributed to the competing influence of the DWD confusion background, which dominates the detector's low-frequency sensitivity band and effectively masks cosmological signals below certain amplitude thresholds in this frequency regime.

Fig. 5 presents the relative uncertainty in amplitude ($\Delta\Omega_{\text{PT}}/\Omega_{\text{PT}}$) while Fig. 6 illustrates the relative uncertainty in peak frequency ($\Delta f_{\text{PT}}/f_{\text{PT}}$) across the parameter space. As expected, $\Delta\Omega_{\text{PT}}/\Omega_{\text{PT}}$ demonstrates a clear inverse relationship with signal strength, decreasing systematically as Ω_{PT} increases due to improved signal-to-noise ratio. Similarly, the fractional uncertainty in frequency determination $\Delta f_{\text{PT}}/f_{\text{PT}}$ also diminishes with increasing signal amplitude. Notably,

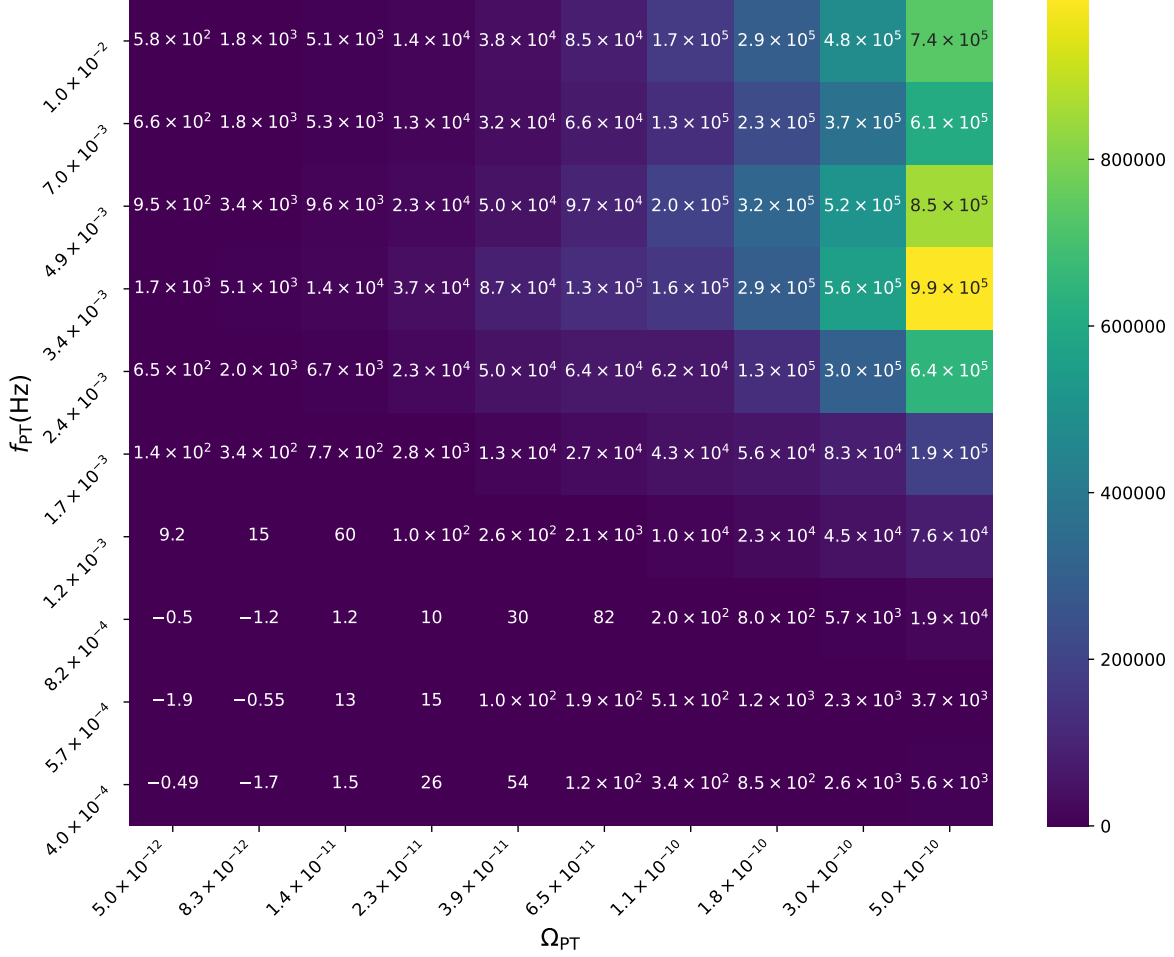


FIG. 7. Model selection analysis using the Bayes factors. The heatmap displays logarithmic Bayes factors comparing models with and without a phase transition component, plotted as a function of signal amplitude (Ω_{PT}) and peak frequency (f_{PT}).

when the phase transition signal reaches $\Omega_{PT} \gtrsim 1.1 \times 10^{-10}$, the frequency can be determined with high precision, achieving $\Delta f_{PT}/f_{PT} \lesssim 0.1$ across most of the frequency range.

To quantitatively evaluate model selection capabilities, we present the logarithmic BFs in Fig. 7 and the DIC differences in Fig. 8, comparing models with and without the phase transition component across the parameter space. Both metrics exhibit consistent behavior, showing progressive improvement in detection confidence as Ω_{PT} increases. This concordance between independent statistical measures reinforces our confidence in the results. The observed trend aligns with theoretical expectations, as larger amplitude signals naturally produce more decisive evidence for the presence of a cosmological phase transition against the null hypothesis of only astrophysical and instrumental backgrounds.

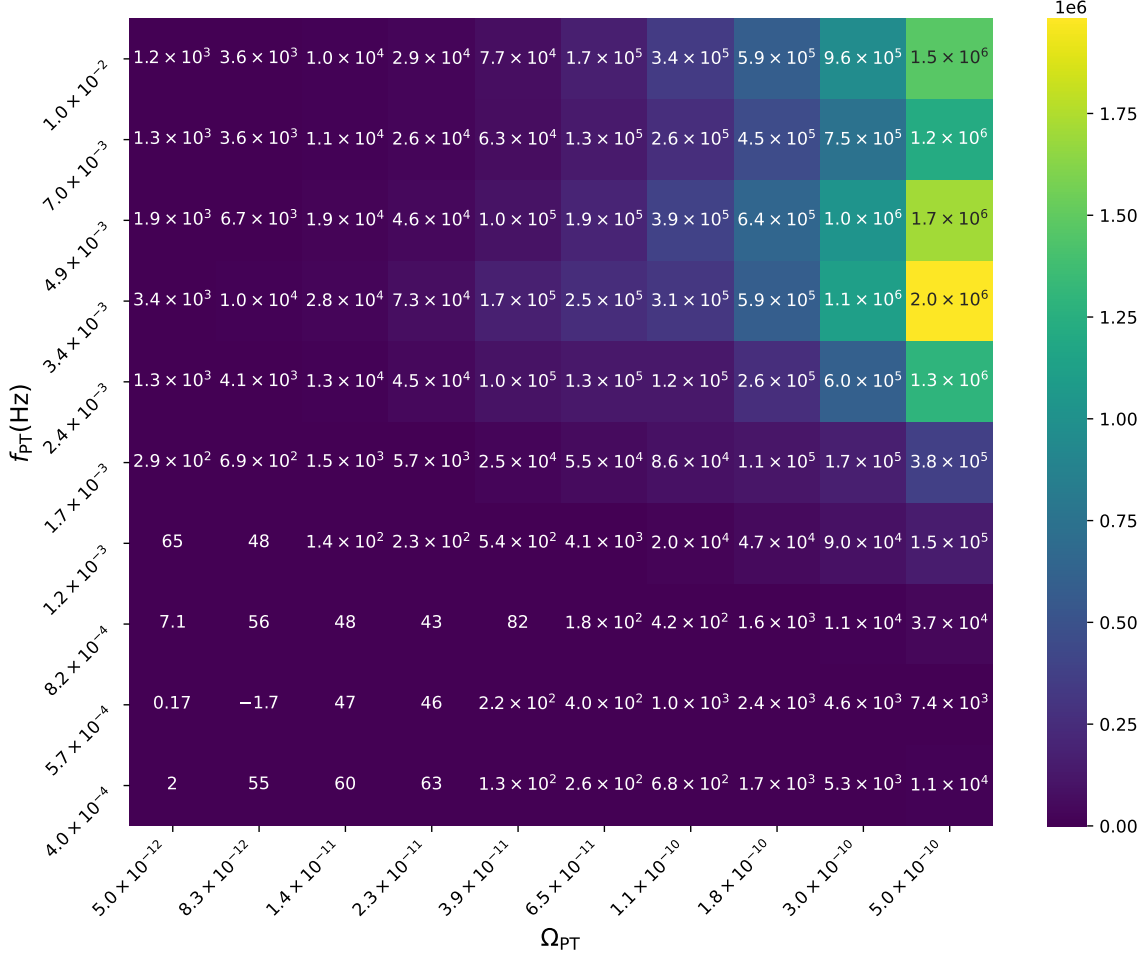


FIG. 8. Model selection analysis using the Deviance Information Criterion (DIC). The heatmap illustrates the difference in DIC values between models with and without a phase transition component across the parameter space of signal amplitude (Ω_{PT}) and characteristic frequency (f_{PT}).

In conclusion, our comprehensive analysis demonstrates Taiji’s significant potential for probing cosmological FOPTs through their GW signatures [71, 72]. The detector shows robust parameter recovery capabilities for signals with amplitudes exceeding $\Omega_{PT} \gtrsim 1.4 \times 10^{-11}$ across most of the frequency range. This sensitivity threshold represents a substantial improvement over current constraints [73, 74] and would enable tests of various early universe scenarios, including strongly supercooled transitions and those associated with composite Higgs models or hidden sector physics [39, 75]. The consistency between our Bayesian evidence calculations and information-theoretic metrics provides a solid statistical foundation for future detection claims [76]. While our study focused on the broken power-law spectral template, future work should explore more physically motivated spectral shapes directly connected to specific phase transition parameters such as

transition temperature, strength, and bubble wall velocity [22, 77]. Additionally, the synergistic potential of Taiji operating concurrently with other space-based detectors like LISA would further enhance detection prospects through cross-correlation techniques [78, 79].

ACKNOWLEDGMENTS

ZCC is supported by the National Natural Science Foundation of China (Grant No. 12405056), the Natural Science Foundation of Hunan Province (Grant No. 2025JJ40006), and the Innovative Research Group of Hunan Province (Grant No. 2024JJ1006). QGH is supported by the grants from National Natural Science Foundation of China (Grant No. 12475065) and China Manned Space Program through its Space Application System. We acknowledge the use of HPC Cluster of ITP-CAS.

-
- [1] B. P. Abbott *et al.* (LIGO Scientific, Virgo), “Observation of Gravitational Waves from a Binary Black Hole Merger,” *Phys. Rev. Lett.* **116**, 061102 (2016), [arXiv:1602.03837 \[gr-qc\]](#).
 - [2] Chiara Caprini and Daniel G. Figueroa, “Cosmological Backgrounds of Gravitational Waves,” *Class. Quant. Grav.* **35**, 163001 (2018), [arXiv:1801.04268 \[astro-ph.CO\]](#).
 - [3] Michele Maggiore, *Gravitational Waves. Vol. 2: Astrophysics and Cosmology* (Oxford University Press, 2018).
 - [4] Edward Witten, “Cosmic Separation of Phases,” *Phys. Rev. D* **30**, 272–285 (1984).
 - [5] C. J. Hogan, “Gravitational radiation from cosmological phase transitions,” *Mon. Not. Roy. Astron. Soc.* **218**, 629–636 (1986).
 - [6] Sidney R. Coleman, “The Fate of the False Vacuum. 1. Semiclassical Theory,” *Phys. Rev. D* **15**, 2929–2936 (1977), [Erratum: *Phys.Rev.D* 16, 1248 (1977)].
 - [7] Andrei D. Linde, “Decay of the False Vacuum at Finite Temperature,” *Nucl. Phys. B* **216**, 421 (1983), [Erratum: *Nucl.Phys.B* 223, 544 (1983)].
 - [8] Mark Hindmarsh, Stephan J. Huber, Kari Rummukainen, and David J. Weir, “Gravitational waves from the sound of a first order phase transition,” *Phys. Rev. Lett.* **112**, 041301 (2014), [arXiv:1304.2433 \[hep-ph\]](#).
 - [9] Mark Hindmarsh, Stephan J. Huber, Kari Rummukainen, and David J. Weir, “Numerical simulations of acoustically generated gravitational waves at a first order phase transition,” *Phys. Rev. D* **92**, 123009 (2015), [arXiv:1504.03291 \[astro-ph.CO\]](#).
 - [10] Ryusuke Jinno and Masahiro Takimoto, “Gravitational waves from bubble collisions: An analytic derivation,” *Phys. Rev. D* **95**, 024009 (2017), [arXiv:1605.01403 \[astro-ph.CO\]](#).

- [11] Mark Hindmarsh, Stephan J. Huber, Kari Rummukainen, and David J. Weir, “Shape of the acoustic gravitational wave power spectrum from a first order phase transition,” *Phys. Rev. D* **96**, 103520 (2017), [Erratum: *Phys.Rev.D* 101, 089902 (2020)], [arXiv:1704.05871 \[astro-ph.CO\]](#).
- [12] Thomas Konstandin, “Gravitational radiation from a bulk flow model,” *JCAP* **03**, 047 (2018), [arXiv:1712.06869 \[astro-ph.CO\]](#).
- [13] Daniel Cutting, Mark Hindmarsh, and David J. Weir, “Vorticity, kinetic energy, and suppressed gravitational wave production in strong first order phase transitions,” *Phys. Rev. Lett.* **125**, 021302 (2020), [arXiv:1906.00480 \[hep-ph\]](#).
- [14] Alberto Roper Pol, Sayan Mandal, Axel Brandenburg, Tina Kahniashvili, and Arthur Kosowsky, “Numerical simulations of gravitational waves from early-universe turbulence,” *Phys. Rev. D* **102**, 083512 (2020), [arXiv:1903.08585 \[astro-ph.CO\]](#).
- [15] Marek Lewicki and Ville Vaskonen, “Gravitational wave spectra from strongly supercooled phase transitions,” *Eur. Phys. J. C* **80**, 1003 (2020), [arXiv:2007.04967 \[astro-ph.CO\]](#).
- [16] Jani Dahl, Mark Hindmarsh, Kari Rummukainen, and David J. Weir, “Decay of acoustic turbulence in two dimensions and implications for cosmological gravitational waves,” *Phys. Rev. D* **106**, 063511 (2022), [arXiv:2112.12013 \[gr-qc\]](#).
- [17] Ryusuke Jinno, Thomas Konstandin, Henrique Rubira, and Isak Stomberg, “Higgsless simulations of cosmological phase transitions and gravitational waves,” *JCAP* **02**, 011 (2023), [arXiv:2209.04369 \[astro-ph.CO\]](#).
- [18] Pierre Auclair, Chiara Caprini, Daniel Cutting, Mark Hindmarsh, Kari Rummukainen, Danièle A. Steer, and David J. Weir, “Generation of gravitational waves from freely decaying turbulence,” *JCAP* **09**, 029 (2022), [arXiv:2205.02588 \[astro-ph.CO\]](#).
- [19] Ramkishor Sharma, Jani Dahl, Axel Brandenburg, and Mark Hindmarsh, “Shallow relic gravitational wave spectrum with acoustic peak,” *JCAP* **12**, 042 (2023), [arXiv:2308.12916 \[gr-qc\]](#).
- [20] Alberto Roper Pol, Simona Procacci, and Chiara Caprini, “Characterization of the gravitational wave spectrum from sound waves within the sound shell model,” *Phys. Rev. D* **109**, 063531 (2024), [arXiv:2308.12943 \[gr-qc\]](#).
- [21] Christophe Grojean and Geraldine Servant, “Gravitational Waves from Phase Transitions at the Electroweak Scale and Beyond,” *Phys. Rev. D* **75**, 043507 (2007), [arXiv:hep-ph/0607107](#).
- [22] Mark B. Hindmarsh, Marvin Lüben, Johannes Lumma, and Martin Pauly, “Phase transitions in the early universe,” *SciPost Phys. Lect. Notes* **24**, 1 (2021), [arXiv:2008.09136 \[astro-ph.CO\]](#).
- [23] V. A. Kuzmin, V. A. Rubakov, and M. E. Shaposhnikov, “On the Anomalous Electroweak Baryon Number Nonconservation in the Early Universe,” *Phys. Lett. B* **155**, 36 (1985).
- [24] Andrew G. Cohen, D. B. Kaplan, and A. E. Nelson, “Progress in electroweak baryogenesis,” *Ann. Rev. Nucl. Part. Sci.* **43**, 27–70 (1993), [arXiv:hep-ph/9302210](#).
- [25] Michael J. Baker, Joachim Kopp, and Andrew J. Long, “Filtered Dark Matter at a First Order Phase Transition,” *Phys. Rev. Lett.* **125**, 151102 (2020), [arXiv:1912.02830 \[hep-ph\]](#).

- [26] Wen-Rui Hu and Yue-Liang Wu, “The Taiji Program in Space for gravitational wave physics and the nature of gravity,” *Natl. Sci. Rev.* **4**, 685–686 (2017).
- [27] Wen-Hong Ruan, Zong-Kuan Guo, Rong-Gen Cai, and Yuan-Zhong Zhang, “Taiji program: Gravitational-wave sources,” *Int. J. Mod. Phys. A* **35**, 2050075 (2020), [arXiv:1807.09495 \[gr-qc\]](#).
- [28] Pau Amaro-Seoane *et al.* (LISA), “Laser Interferometer Space Antenna,” (2017), [arXiv:1702.00786 \[astro-ph.IM\]](#).
- [29] Jun Luo *et al.* (TianQin), “TianQin: a space-borne gravitational wave detector,” *Class. Quant. Grav.* **33**, 035010 (2016), [arXiv:1512.02076 \[astro-ph.IM\]](#).
- [30] Alison J. Farmer and E. Sterl Phinney, “The gravitational wave background from cosmological compact binaries,” *Mon. Not. Roy. Astron. Soc.* **346**, 1197 (2003), [arXiv:astro-ph/0304393](#).
- [31] Ashley J. Ruiter, Krzysztof Belczynski, Matthew Benacquista, Shane L. Larson, and Gabriel Williams, “The LISA Gravitational Wave Foreground: A Study of Double White Dwarfs,” *Astrophys. J.* **717**, 1006–1021 (2010), [arXiv:0705.3272 \[astro-ph\]](#).
- [32] Xing-Jiang Zhu, Eric J. Howell, David G. Blair, and Zong-Hong Zhu, “On the gravitational wave background from compact binary coalescences in the band of ground-based interferometers,” *Mon. Not. Roy. Astron. Soc.* **431**, 882–899 (2013), [arXiv:1209.0595 \[gr-qc\]](#).
- [33] Pablo A. Rosado, “Gravitational wave background from binary systems,” *Phys. Rev. D* **84**, 084004 (2011), [arXiv:1106.5795 \[gr-qc\]](#).
- [34] G. Nelemans, L. R. Yungelson, and Simon F. Portegies Zwart, “The gravitational wave signal from the galactic disk population of binaries containing two compact objects,” *Astron. Astrophys.* **375**, 890–898 (2001), [arXiv:astro-ph/0105221](#).
- [35] Tania Regimbau, “The astrophysical gravitational wave stochastic background,” *Res. Astron. Astrophys.* **11**, 369–390 (2011), [arXiv:1101.2762 \[astro-ph.CO\]](#).
- [36] Joseph D. Romano and Neil J. Cornish, “Detection methods for stochastic gravitational-wave backgrounds: a unified treatment,” *Living Rev. Rel.* **20**, 2 (2017), [arXiv:1608.06889 \[gr-qc\]](#).
- [37] Neil Cornish and Travis Robson, “Galactic binary science with the new LISA design,” *J. Phys. Conf. Ser.* **840**, 012024 (2017), [arXiv:1703.09858 \[astro-ph.IM\]](#).
- [38] Chiara Caprini *et al.*, “Science with the space-based interferometer eLISA. II: Gravitational waves from cosmological phase transitions,” *JCAP* **04**, 001 (2016), [arXiv:1512.06239 \[astro-ph.CO\]](#).
- [39] Chiara Caprini *et al.*, “Detecting gravitational waves from cosmological phase transitions with LISA: an update,” *JCAP* **03**, 024 (2020), [arXiv:1910.13125 \[astro-ph.CO\]](#).
- [40] Chloe Gowling and Mark Hindmarsh, “Observational prospects for phase transitions at LISA: Fisher matrix analysis,” *JCAP* **10**, 039 (2021), [arXiv:2106.05984 \[astro-ph.CO\]](#).
- [41] Chloe Gowling, Mark Hindmarsh, Deanna C. Hooper, and Jesús Torrado, “Reconstructing physical parameters from template gravitational wave spectra at LISA: first order phase transitions,” *JCAP* **04**, 061 (2023), [arXiv:2209.13551 \[astro-ph.CO\]](#).

- [42] Guillaume Boileau, Nelson Christensen, Chloe Gowling, Mark Hindmarsh, and Renate Meyer, “Prospects for LISA to detect a gravitational-wave background from first order phase transitions,” *JCAP* **02**, 056 (2023), [arXiv:2209.13277 \[gr-qc\]](#).
- [43] Chiara Caprini, Ryusuke Jinno, Marek Lewicki, Eric Madge, Marco Merchand, Germano Nardini, Mauro Pieroni, Alberto Roper Pol, and Ville Vaskonen (LISA Cosmology Working Group), “Gravitational waves from first-order phase transitions in LISA: reconstruction pipeline and physics interpretation,” *JCAP* **10**, 020 (2024), [arXiv:2403.03723 \[astro-ph.CO\]](#).
- [44] Mark Hindmarsh, Deanna C. Hooper, Tiina Minkkinen, and David J. Weir, “Recovering a phase transition signal in simulated LISA data with a modulated galactic foreground,” (2024), [arXiv:2406.04894 \[astro-ph.CO\]](#).
- [45] Adam Gonstal, Marek Lewicki, and Bogumila Swiezevska, “Reconstructing early universe evolution with gravitational waves from supercooled phase transitions,” (2025), [arXiv:2502.18436 \[gr-qc\]](#).
- [46] Wen-Hong Ruan, Chang Liu, Zong-Kuan Guo, Yue-Liang Wu, and Rong-Gen Cai, “The LISA-Taiji Network: Precision Localization of Coalescing Massive Black Hole Binaries,” *Research* **2021**, 6014164 (2021), [arXiv:1909.07104 \[gr-qc\]](#).
- [47] Wen-Hong Ruan, Chang Liu, Zong-Kuan Guo, Yue-Liang Wu, and Rong-Gen Cai, “The LISA-Taiji network,” *Nature Astron.* **4**, 108–109 (2020), [arXiv:2002.03603 \[gr-qc\]](#).
- [48] Renjie Wang, Wen-Hong Ruan, Qing Yang, Zong-Kuan Guo, Rong-Gen Cai, and Bin Hu, “Hubble parameter estimation via dark sirens with the LISA-Taiji network,” *Natl. Sci. Rev.* **9**, nwab054 (2022), [arXiv:2010.14732 \[astro-ph.CO\]](#).
- [49] Ling-Feng Wang, Shang-Jie Jin, Jing-Fei Zhang, and Xin Zhang, “Forecast for cosmological parameter estimation with gravitational-wave standard sirens from the LISA-Taiji network,” *Sci. China Phys. Mech. Astron.* **65**, 210411 (2022), [arXiv:2101.11882 \[gr-qc\]](#).
- [50] Bo-Rui Wang and Jin Li, “Ability of LISA, Taiji, and their networks to detect the stochastic gravitational wave background generated by cosmic strings,” *Phys. Rev. D* **109**, 063520 (2024), [arXiv:2311.07116 \[astro-ph.CO\]](#).
- [51] Shang-Jie Jin, Ye-Zhu Zhang, Ji-Yu Song, Jing-Fei Zhang, and Xin Zhang, “Taiji-TianQin-LISA network: Precisely measuring the Hubble constant using both bright and dark sirens,” *Sci. China Phys. Mech. Astron.* **67**, 220412 (2024), [arXiv:2305.19714 \[astro-ph.CO\]](#).
- [52] Rong-Gen Cai, Zong-Kuan Guo, Bin Hu, Chang Liu, Youjun Lu, Wei-Tou Ni, Wen-Hong Ruan, Naoki Seto, Gang Wang, and Yue-Liang Wu, “On networks of space-based gravitational-wave detectors,” *Fund. Res.* **4**, 1072–1085 (2024), [arXiv:2305.04551 \[gr-qc\]](#).
- [53] Zheng-Cheng Liang, Zhi-Yuan Li, En-Kun Li, Jian-dong Zhang, and Yi-Ming Hu, “Unveiling a multicomponent stochastic gravitational-wave background with the TianQin+LISA network,” *Phys. Rev. D* **111**, 043032 (2025), [arXiv:2409.00778 \[gr-qc\]](#).
- [54] N. Aghanim *et al.* (Planck), “Planck 2018 results. VI. Cosmological parameters,” *Astron. Astrophys.* **641**, A6 (2020), [Erratum: *Astron. Astrophys.* 652, C4 (2021)], [arXiv:1807.06209 \[astro-ph.CO\]](#).

- [55] Massimo Tinto, J. W. Armstrong, and F. B. Estabrook, “Discriminating a gravitational wave background from instrumental noise in the LISA detector,” *Phys. Rev. D* **63**, 021101 (2001).
- [56] Massimo Tinto, F. B. Estabrook, and J. W. Armstrong, “Time delay interferometry for LISA,” *Phys. Rev. D* **65**, 082003 (2002).
- [57] Jun Luo *et al.*, “The first round result from the TianQin-1 satellite,” *Class. Quant. Grav.* **37**, 185013 (2020), [arXiv:2008.09534 \[physics.ins-det\]](#).
- [58] Zhixiang Ren, Tianyu Zhao, Zhoujian Cao, Zong-Kuan Guo, Wen-Biao Han, Hong-Bo Jin, and Yue-Liang Wu, “Taiji data challenge for exploring gravitational wave universe,” *Front. Phys. (Beijing)* **18**, 64302 (2023), [arXiv:2301.02967 \[gr-qc\]](#).
- [59] Ziren Luo, ZongKuan Guo, Gang Jin, Yueliang Wu, and Wenrui Hu, “A brief analysis to Taiji: Science and technology,” *Results Phys.* **16**, 102918 (2020).
- [60] Thomas A. Prince, Massimo Tinto, Shane L. Larson, and J. W. Armstrong, “The LISA optimal sensitivity,” *Phys. Rev. D* **66**, 122002 (2002), [arXiv:gr-qc/0209039](#).
- [61] Pan-Pan Wang, Yu-Jie Tan, Wei-Liang Qian, and Cheng-Gang Shao, “Sensitivity functions of spaceborne gravitational wave detectors for arbitrary time-delay interferometry combinations regarding non-tensorial polarizations,” *Phys. Rev. D* **104**, 023002 (2021).
- [62] V. Korol *et al.*, “Populations of double white dwarfs in Milky Way satellites and their detectability with LISA,” *Astron. Astrophys.* **638**, A153 (2020), [arXiv:2002.10462 \[astro-ph.GA\]](#).
- [63] Valeriya Korol, Na’ama Hallakoun, Silvia Toonen, and Nikolaos Karnesis, “Observationally driven Galactic double white dwarf population for LISA,” *Mon. Not. Roy. Astron. Soc.* **511**, 5936–5947 (2022), [arXiv:2109.10972 \[astro-ph.HE\]](#).
- [64] Nikolaos Karnesis, Stanislav Babak, Mauro Pieroni, Neil Cornish, and Tyson Littenberg, “Characterization of the stochastic signal originating from compact binary populations as measured by LISA,” *Phys. Rev. D* **104**, 043019 (2021), [arXiv:2103.14598 \[astro-ph.IM\]](#).
- [65] Chang Liu, Wen-Hong Ruan, and Zong-Kuan Guo, “Confusion noise from Galactic binaries for Taiji,” *Phys. Rev. D* **107**, 064021 (2023), [arXiv:2301.02821 \[astro-ph.IM\]](#).
- [66] Zu-Cheng Chen, Qing-Guo Huang, Chang Liu, Lang Liu, Xiao-Jin Liu, You Wu, Yu-Mei Wu, Zhu Yi, and Zhi-Qiang You, “Prospects for Taiji to detect a gravitational-wave background from cosmic strings,” *JCAP* **03**, 022 (2024), [arXiv:2310.00411 \[astro-ph.IM\]](#).
- [67] Zu-Cheng Chen and Lang Liu, “Detecting a gravitational wave background from inflation with null energy condition violation: prospects for Taiji,” *Eur. Phys. J. C* **84**, 1176 (2024), [arXiv:2404.08375 \[gr-qc\]](#).
- [68] Zu-Cheng Chen, Fan Huang, and Qing-Guo Huang, “Stochastic Gravitational-wave Background from Binary Black Holes and Binary Neutron Stars and Implications for LISA,” *Astrophys. J.* **871**, 97 (2019), [arXiv:1809.10360 \[gr-qc\]](#).
- [69] Chiara Caprini, Daniel G. Figueroa, Raphael Flauger, Germano Nardini, Marco Peloso, Mauro Pieroni, Angelo Ricciardone, and Gianmassimo Tasinato, “Reconstructing the spectral shape of a stochastic

- gravitational wave background with LISA,” *JCAP* **11**, 017 (2019), [arXiv:1906.09244 \[astro-ph.CO\]](#).
- [70] Raphael Flauger, Nikolaos Karnesis, Germano Nardini, Mauro Pieroni, Angelo Ricciardone, and Jesús Torrado, “Improved reconstruction of a stochastic gravitational wave background with LISA,” *JCAP* **01**, 059 (2021), [arXiv:2009.11845 \[astro-ph.CO\]](#).
- [71] Wen-Hong Ruan, Zong-Kuan Guo, Rong-Gen Cai, and Yuan-Zhong Zhang, “Taiji program: Gravitational-wave sources,” *Int. J. Mod. Phys. A* **35**, 2050075 (2020), [arXiv:1807.09495 \[gr-qc\]](#).
- [72] Hai-Tian Wang *et al.*, “Science with the TianQin observatory: Preliminary results on massive black hole binaries,” *Phys. Rev. D* **100**, 043003 (2019), [arXiv:1902.04423 \[astro-ph.HE\]](#).
- [73] Gabriella Agazie *et al.* (NANOGrav), “The NANOGrav 15 yr Data Set: Evidence for a Gravitational-wave Background,” *Astrophys. J. Lett.* **951**, L8 (2023), [arXiv:2306.16213 \[astro-ph.HE\]](#).
- [74] J. Antoniadis *et al.* (EPTA, InPTA:), “The second data release from the European Pulsar Timing Array - III. Search for gravitational wave signals,” *Astron. Astrophys.* **678**, A50 (2023), [arXiv:2306.16214 \[astro-ph.HE\]](#).
- [75] John Ellis, Marek Lewicki, and José Miguel No, “Gravitational waves from first-order cosmological phase transitions: lifetime of the sound wave source,” *JCAP* **07**, 050 (2020), [arXiv:2003.07360 \[hep-ph\]](#).
- [76] Neil J. Cornish and Laura Sampson, “Towards Robust Gravitational Wave Detection with Pulsar Timing Arrays,” *Phys. Rev. D* **93**, 104047 (2016), [arXiv:1512.06829 \[gr-qc\]](#).
- [77] Daniel Cutting, Elba Granados Escartin, Mark Hindmarsh, and David J. Weir, “Gravitational waves from vacuum first order phase transitions II: from thin to thick walls,” *Phys. Rev. D* **103**, 023531 (2021), [arXiv:2005.13537 \[astro-ph.CO\]](#).
- [78] Giorgio Orlando, Mauro Pieroni, and Angelo Ricciardone, “Measuring Parity Violation in the Stochastic Gravitational Wave Background with the LISA-Taiji network,” *JCAP* **03**, 069 (2021), [arXiv:2011.07059 \[astro-ph.CO\]](#).
- [79] Zheng-Cheng Liang, Yi-Ming Hu, Yun Jiang, Jun Cheng, Jian-dong Zhang, and Jianwei Mei, “Science with the TianQin Observatory: Preliminary results on stochastic gravitational-wave background,” *Phys. Rev. D* **105**, 022001 (2022), [arXiv:2107.08643 \[astro-ph.CO\]](#).